UCLA
UCLA Previously Published Works

Title
Cardiac Magnetic Resonance Quantification of Structure-Function Relationships in Heart Failure.

Permalink
https://escholarship.org/uc/item/4pz558bx

Journal
Heart failure clinics, 17(1)

ISSN
1551-7136

Authors
Nguyen, Kim-Lien
Hu, Peng
Finn, J Paul

Publication Date
2021

DOI
10.1016/j.hfc.2020.08.001

Peer reviewed

CMR Quantification of Structure-Function Relationships in Heart Failure

Kim-Lien Nguyen, MD[1,2,3], **Peng Hu, PhD**[2,3], **J. Paul Finn, MD**[2,3]

[1]Division of Cardiology, David Geffen School of Medicine at UCLA and VA Greater Los Angeles Healthcare System

[2]Diagnostic Cardiovascular Imaging Research Laboratory, Department of Radiology, David Geffen School of Medicine at UCLA

[3]Physics & Biology in Medicine Graduate Program, University of California, Los Angeles

Abstract

Classification of heart failure is based on the left ventricular ejection fraction (LVEF): preserved EF, mid-range EF, and reduced EF. There remains an unmet need for further heart failure phenotyping of ventricular structure-function relationships. Due to high spatiotemporal resolution, cardiac magnetic resonance (CMR) remains the reference modality for quantification of ventricular contractile function. Recent technical advancements in CMR have shifted the paradigm for quantification of ventricular function beyond the EF to include myocardial mechanics, in vivo tissue microstructure, and intraventricular flow analysis. Advanced methods in image reconstruction, post-processing, and off-label use of iron-based contrast agents such as ferumoxytol have enhanced the clinical CMR workflow. We aim to highlight novel frameworks including theranostic use of ferumoxytol to enable more efficient evaluation of ventricular function in heart failure patients who are also frequently anemic, and to discuss emerging quantitative CMR approaches for evaluation of ventricular structure-function relationships in heart failure.

Keywords

heart failure; cardiovascular magnetic resonance; strain; diffusion tensor; 4D flow; cardiac function and morphology; myocardial microstructure; ferumoxytol

INTRODUCTION

Heart failure (HF) affects approximately 6.5 million adults in the U.S. and is expected to increase in prevalence due to an aging population and cardiometabolic disorders.[1] Although imperfect, the left ventricular ejection fraction (LVEF) serves as a surrogate marker for combined LV function and structural phenotyping of HF. Current classification of HF is

based solely on the EF and can be divided into 1) HF with preserved EF (HFpEF, LVEF 50%), 2) reduced EF (HFrEF, LVEF <40%, and 3) mid-range EF (HFmrEF, LVEF 40–49%). Echocardiography is the mainstay of initial LVEF assessment in patients who present with signs and symptoms of HF. However, cardiovascular magnetic resonance (CMR) imaging serves as the standard reference modality for quantification of ventricular volume, global and regional contractile function, and ventricular mass because of its high spatiotemporal resolution. In the past decade however, advances in CMR have shifted the paradigm beyond quantification of ventricular EF to provide other quantitative signatures of ventricular function.

Most recently, the use of LVEF to categorize cardiomyopathies and to serve as a proxy for contractility in the failing heart has been called into question due to dependency of LVEF on load and heart rate as well as interobserver variability when derived from 2D cardiac ultrasound.[2] Historically, the concept of ventricular EF arose from development of angiographic techniques to reliably measure stroke volume. Kennedy et al[3] first defined the EF as the stroke volume divided by end-diastolic volume (or the ejected ventricular volume). Sonnenblick et al[4] later demonstrated EF to be related to sarcomere shortening. Together, these findings serve as the basis for historical and current use of LVEF as a measurement of contractile function. As a measure for diagnosis, prognosis, treatment, and development of new therapeutics, the LVEF has stood the test of time through its strong inverse association with mortality and its prediction of both clinical outcomes and therapeutic response across a wide range of patients and disease states.

One unmet area in HF phenomapping where CMR stands to fill a large gap is HFpEF and HFmrEF. Beyond ventricular function, volume, and mass, CMR can provide additional information on tissue characteristics, perfusion, myocardial mechanics, tissue microarchitecture, and intraventricular blood flow patterns. Excellent, detailed discussions of technical CMR principles[5, 6] and imaging protocols[7, 8] are available in the published literature. In this work, we provide a summary of technical advances in novel CMR methods to improve quantitative assessment of ventricular contractile structure-function relationships.

VENTRICULAR STRUCTURE-FUNCTION RELATIONSHIP

The relationship between myocardial architecture and ventricular function is complex. Myocardial deformation, microstructural orientation, and LV shape contribute to the overall EF. Ventricular contraction occurs along the longitudinal axis with circumferential shortening and radial thickening. From the LV apex to base, cardiomyocytes have a left-handed helical course at the epicardium, transitioning to circumferential arrangements at the mid-myocardium, and turning towards a right-handed helical pattern at the endocardium.[9] The helical arrangement contributes to myocardial rotation and torsion during contraction. Cardiomyocytes serve as fundamental contractile elements and only shorten by ~15% and thicken by ~8% during systole. Secondary organization of myocytes consist of laminar structures (~5–10 cardiomyocytes thick) termed sheets[10] or sheetlets that are surrounded by collagen and multiple other local subpopulations of counter-sloping sheetlets (shear layers). [11] Together, the reorientation of the sheetlets and shear layer slippage serve as the main contributors to LV wall thickening and base-to-apex systolic shortening.

THERANOSTIC USE OF FERUMOXYTOL IN HEART FAILURE

Thirty to 50% of HF patients have anemia of chronic disease.[12] Guidelines[13] and expert opinions[14] recommend intravenous rather than oral iron repletion because supplementation has been shown to improve exercise capacity, HF symptoms, and health-related quality of life; yet, not all patients are adequately treated. Many HF patients also have concomitant cardiorenal disease, which limit the use of gadolinium-based MR contrast agents. Even in the absence of renal dysfunction, data have emerged to support accumulation of gadolinium in brain and other tissues.[15, 16] CMR with cine imaging is typically performed without contrast agents. However, some techniques to further characterize ventricular function may benefit from contrast enhancement. Contrast agents with paramagnetic properties are used in CMR imaging to modify the T1, T2, and T2* relaxation times of local tissues and the relative effects are visualized as tissue contrast using different CMR pulse sequences. In the context of HF where patients have anemia and renal dysfunction, ferumoxytol (Feraheme, AMAG Pharmaceuticals, Waltham, MA), may be used on-label for therapeutic (treatment of anemia)[14, 17] and off-label for diagnostic purposes.[18–21] Ferumoxytol is an intravenous iron-oxide nanoparticle that has been approved by the U.S. Food and Drug Administration for treatment of iron deficiency anemia and was originally developed as an MR contrast agent, [22, 23] but manufacturers eventually pursued a therapeutic indication. As an ultrasmall, superparamagnetic, iron-oxide nanoparticle with an intravascular half-life of 14–15 hours and a high r_1 of 15 L mmol^{-1}s^{-1}, ferumoxytol is predominantly an intravascular contrast agent, but its biodistribution and metabolism by the reticuloendothelial system can be leveraged for a variety of imaging indications[18–21, 24] beyond the current capabilities of commercially available gadolinium-based contrast agents (Fig. 1). The long half-life enables a long temporal window for high-resolution, high signal-to-noise (SNR) vascular imaging[20, 21] while delayed imaging at later time points (1–10 days post-injection) enable tracking of macrophage activity.[25–27] Despite its promising applications, ferumoxytol received an FDA black-box warning for potential anaphylactic allergic reactions related to its post-marketing therapeutic use.[28] With vigilant monitoring of vital signs, dilution, and slow infusion, no further reports of fatal anaphylaxis allergic reactions have been reported. In contrast, the diagnostic use of ferumoxytol has shown favorable safety profile in both single-center[29–32] and multicenter reports.[33] The total amount of ferumoxytol used for diagnostic purposes is typically less than half the therapeutic dose. Several caveats merit mention: 1) high ferumoxytol concentration may be associated with susceptibility artifacts, 2) effects may be present on MR images for up to 6 months, and 3) dilution factor and short echo time must be carefully chosen for specific indications.

VENTRICULAR EJECTION FRACTION, VOLUME, AND MASS

2-Dimensional Imaging.

Conventional quantification of ventricular volume, ejection fraction, and mass is derived from a stack of breath-held, 2D multi-slice, short-axis, cine MR images acquired from the ventricular base to apex. Each 2D slice is 6–8mm in thickness and the interslice gap is 2–4mm. The segmented raw image data are acquired for each cardiac phase of every cardiac cycle and takes a total of 6–7 minutes if acceleration approaches are used. Images are

typically acquired at end-expiration to ensure consistent cardiac positioning within the thoracic cavity. The data are then averaged to generate a movie (typically 25–30 frames, Fig. 1). Acquisition of cine images can be performed using spoiled-gradient echo fast low-angle shot (FLASH)[34] or balanced steady-state free precession (bSSFP)[35, 36] pulse sequences. FLASH relies on blood inflow to generate blood-myocardial contrast and has low contrast-to-noise (CNR), especially at short repetition times (TR) and with low flow rates. bSSFP is based on steady state signal (T2 to T1 ratio) and remains the cornerstone for cine MR imaging. Relative to FLASH, bSSFP has higher in-plane resolution with shorter acquisition time and better overall image quality. Shorter TR is possible with SSFP while maintaining consistent high blood-myocardial contrast. However, SSFP tends to yield slightly higher LV end-diastolic volume (EDV, 13.3±11.6mL, p<0.0001) and end-systolic volume (ESV, 12.2±11.7mL, p<0.0001) with lower ventricular mass (21.5±10.1g, p<0.0001).[37, 38] LVEF by SSFP is slightly lower relative to LVEF by gradient echo (3.8±4.6%, p<0.0001); differences in LV stroke volume is negligible (0.7±11.6mL, p=0.69).

Image Acceleration.

To improve overall scan time, several acceleration strategies[39–41] may be employed to speed up image acquisition and to reduce the acquisition of each 2D cine slice to 4–5 seconds. These approaches all involve some form of data undersampling and can be classified as parallel imaging, prior-knowledge-driven imaging including several k-t methods[42], and compressed sensing. Of these approaches, parallel imaging is most widely used and two variants are commercially available: sensitivity encoding (SENSE) and GeneRalized Autocalibrating Partially Parallel Acquisitions (GRAPPA). SENSE formulates the image reconstruction problem as an inverse problem and leverages intrinsic redundancies in multi-coil image encoding to recover the image from under-sampled k-space data. While parallel imaging along with improved coil arrays can reduce scan time by three- to four-fold, prior-knowledge-driven approaches or the combination of prior-knowledge-driven and parallel imaging can achieve higher acceleration relative to parallel imaging alone. The latter combination of approaches is especially important for dynamic imaging such as cardiac cine imaging because these methods leverage close correlation between dynamic frames to achieve greater k-space undersampling. With acceleration however, tradeoffs between acceleration and occurrence of artifacts need to be considered. For parallel imaging, SNR and contrast-to-noise ratios (CNR) used in image quality comparisons may require consideration of spatially varying noise whereas temporal fidelity of images reconstructed from certain knowledge-driven methods need further validation.

In compressed sensing[43] the transform domain L1-norm minimization using non-linear optimization methods are applied at the time of image reconstruction to take advantage of the intrinsic data sparsity of medical images in a pre-defined transform domain, such as wavelet. Compressed sensing theory does not require multi-coil MRI data. However, practical implementations of compressed sensing sometimes combines the L1-norm minimization with a k-space data consistency measure based on multi-coil data and its associated data redundancy.[44] Whole-heart, cine CMR with compressed sensing is commercially available on more recent state-of-the-art scanners and can be completed in a single breath-hold.[45] Relative to conventional multislice breath-held SSFP, whole-heart,

single-breath-held SSFP using compressed sensing yields an LVEF mean difference of 1.3±4.3% (p=0.11), LV ESV mean difference of 2.0±11.7mL (p=0.24), LV EDV mean difference of 9.9±10.2mL (p=0.0009), LV stroke volume mean difference of 8.8±12.8mL (p=0.11), and LV mass mean difference of −2.5± 9.6g (p=0.18).[45] With compressed sensing and incorporation of machine-learning methods including deep neural networks, further efficiency may be achieved.[41]

3- and 4-Dimensional Imaging.

Potential gains from 3D imaging with wider field of view have led to increased interest in 4D (3D + cardiac phase-resolved) CMR techniques.[46–61] For conventional CMR scans, multiple additional 2D breath-held slices are acquired in customized imaging planes to answer specific clinical questions in addition to a stack of 2D short axis cine images. Incorporation of isotropic, non-angulated 3D CMR acquisitions with parallel and undersampling reconstruction and respiratory gating has been incorporated into several strategies of 2D and 3D sequences[62–64] to create whole-heart 3D imaging. With newer 4D CMR techniques, the resulting whole-heart cine images can be interrogated in any arbitrary imaging plane after image acquisition and inline reconstruction. While promising, these approaches are not yet commercially available because vendors have not perceived demand by users and insufficient cost-benefit analyses are available. One set of techniques, 4D MUltiphase Steady-state Imaging with Contrast (MUSIC),[52] and its sister, self-gated 4D MUltiphase Steady-state Imaging with Contrast Using ROtating Cartesian K-space (ROCK-MUSIC),[53, 55, 65] has demonstrated technical feasibility and early value in patients with congenital heart disease,[54] especially in neonates and very young children. MUSIC and ROCK-MUSIC leverage the off-label use of ferumoxytol contrast to achieve submillimeter isotropic in-plane spatial resolution (Fig. 2). MUSIC uses the ventilator signal for gating while ROCK-MUSIC is a free-breathing imaging technique. Both are effective for generating high-resolution 4D cine images inclusive of both the beating heart and relevant pulsatile thoraco-abdominal vessels within 5–10 minutes, which depends on the required temporal resolution. Availability of 3D and 4D datasets of ventricular function has paved the way for image-based computational models of cardiac structure and function in several disease states through advanced applications such as statistical shape modeling.[66, 67]

5-Dimensional Imaging.

Most recently, a framework for free-breathing MRI was developed which may offer simultaneous evaluation of cardiopulmonary physiology: eXtra-Dimensional Golden-angle RAdial Sparse Parallel (XD-GRASP) imaging.[68] XD-GRASP builds upon iGRASP[69] whereby continuous multidimensional data are acquired and then sorted into undersampled datasets with distinct motion-states. Compressed sensing is used to reconstruct the motion-sorted datasets from radial k-space data. The extra dimensions may provide additional physiological information, which can be extracted during reconstruction. Based on a 5D whole-heart sparse imaging framework,[70] simultaneous evaluation of myocardial motion and high-resolution cardiac and respiratory motion-resolved acquisitions can be achieved in a single continuous non-contrast exam. These techniques were applied to a 4D flow sequence (XD flow) for simultaneous assessment of cardiopulmonary physiology and where information about ventricular function can be extracted from the anatomic images.[71]

Real-time Imaging.

Patients with heart failure frequently have irregular heart rhythms or difficulty with breath-holding; in these cases, real-time cine CMR may be employed. Feasibility of real-time CMR[72, 73] was facilitated by exploitation of nonlinear algorithms, which has progressed to encompass modified use of radial sampling,[74] parallel imaging,[75, 76] sparse sampling with iterative reconstruction,[77–80] compressed sensing,[81, 82] and unsupervised motion-corrected reconstruction (MOCO-RT).[83] Real-time cine CMR used a fast low-angle single-shot acquisition approach,[72, 73] but more recently has transitioned to bSSFP[80, 83] to improve the SNR as well as spatiotemporal characteristics. The MOCO-RT technique relies on bSSFP, free-breathing, Cartesian, real-time cine acquisition with GRAPPA, and inline unsupervised motion correction. Relative to conventional segmented 2D bSSFP cine, MOCO-RT yields an LVEF mean difference of 1.9% (95% CI −1.9 to 5.6%), LV ESV mean difference of −4.9mL (95% CI −15.6 to 5.8mL), LV EDV mean difference of −5.8mL (95% CI −26.7 to 15.0mL). Compared to other approaches for real-time cine imaging, the MOCO-RT technique's inline reconstruction makes it a more clinically relevant technique with potential for widespread adoption.

Post-processing of Cine Images.

Commercially available software can be used to segment and quantify ventricular volume, ejection fraction, and mass from multi-slice 2D cine images. The routine use of commercial software to analyze 4D datasets remain in the research realm. Potential sources for variability in ventricular volumes merit consideration. The most common error for variability in volumes is selection of the basal short axis slice, which is defined as the most basal slice whereby 50% of the slice's circumference consists of myocardium. This error is offset by using a combination of long-axis and short-axis images when selecting the most basal short-axis slice. Other sources of error include endocardial and epicardial contouring, inexperienced operators, and lack of standardization within an imaging lab. More recent iterations of commercially available CMR processing software have incorporated artificial intelligence into segmentation algorithms to further reduce variability and sources of error. Post-processing of 4D and 5D datasets rely on in-house methods and few commercially available software currently accommodate these data for clinical workflow.

GLOBAL AND REGIONAL MYOCARDIAL MECHANICS

Ventricular structure and function relationships can also be further characterized by quantifying myocardial strain and tissue velocities from myocardial tagging, tissue displacement, and tissue phase mapping techniques.[84] Global and regional myocardial contractility can be described through measures of longitudinal, circumferential, and radial strain and strain rate as well as rotational mechanics including torsion and twist using tagging or tissue displacement imaging. Myocardial tagging[85, 86] involves labeling segments of the ventricular myocardium with dark bands that are perpendicular to the imaging planes to create grid or linear patterns (Fig. 3). Tagging can be done in Cartesian or in polar coordinates.[87] The latter is a better for the ventricular shape and enables higher density of tag lines that are either in the circular or radial direction. The evolution of tagging CMR pulse sequences is nicely outlined by Ibrahim et al.[86] "Tags" are applied at the onset of the R

wave, deform throughout the cardiac cycle, and enable both visualization and quantification of global and regional strain and strain rate. One drawback is fading of the tags as magnetization recovers towards equilibrium due to spin-lattice relaxation throughout the cardiac cycle, especially near end-diastole. Binomial rectilinear grid tags are limited by spatial limits between the tag lines. Other challenges include lack of widely affordable and available commercial software for analyzing specific types of tag lines for strain measurements. Although 3D tagging is possible as a research tool, most clinical CMR workflow rely on 2D myocardial tagging.

Tissue displacement techniques[86] such as displacement encoding with simulated echoes (DENSE), strain encoding (SENC), or feature tracking[88, 89] can also be used for derivation of global and regional strain. DENSE displays tissue motion information at the pixel level; the vector orientation and length reflect direction and magnitude, respectively. Unlike DENSE, SENC, or tagging techniques, feature tracking is a post-processing technique that is applied retrospectively to routinely acquired cine images for derivation of strain measurements (Fig. 3). Feature tracking software tracks endocardial features after user-defined epicardial and endocardial borders are delineated. Global longitudinal strain is derived from three long axis cine images while global circumferential and radial strain are derived from short axis cine images. Relative to conventional tagging or other tissue displacement techniques, feature tracking has been more widely incorporated into routine clinical CMR workflow because of its simplicity and post-processing is possible with several commercially available CMR quantification software. Limitations of feature tracking include pixel size (displacement smaller than the pixel size may not be detected), artefacts from through plane motion, and 2D tracking. Global strain values are more reproducible than regional strain with the most consistent parameter being global longitudinal strain. Global circumferential and longitudinal strain values less negative than −17% or −20%, respectively, are considered pathologic. In patients with HFpEF (n=206), feature tracking derived global longitudinal strain was associated with HF hospitalizations and cardiovascular death (hazard ratio 1.06% per 1% strain increase, 95% confidence interval 1.01–1.11, p=0.03).[90] These findings are consistent with a larger, multicenter study (n=1274) showing global longitudinal strain derived from feature tracking is an independent predictor of all-cause mortality in patients with HFpEF; each 1% worsening in global longitudinal strain was associated with a 22.8% increased risk of death after adjusting for clinical and other imaging factors.[91] The impact of using feature tracking derived global longitudinal strain extends to stress testing. In patients with known or suspected coronary artery disease, blunted global longitudinal strain at peak vasodilator stress perfusion CMR independently predicted major adverse cardiovascular events (death, nonfatal myocardial infarction, heart failure hospitalization, sustained ventricular tachycardia, and late revascularization).[92]

DIFFUSION TENSOR FOR TISSUE MICROSTRUCTURE

Myocardial microstructure is crucial to ventricular architecture, shape, and overall contractile function.[93, 94] Until diffusion tensor (DT) CMR was available, *in vivo* dynamic evaluation of cardiac microstructure in the mammalian heart was not possible. Developments in DT MR have been most robust in neuroimaging, but Edelman et al,[95] in

1994, was able to overcome cardiac bulk motion using a stimulated echo acquisition mode (STEAM) technique to capture the first *in vivo* diffusion cardiac images. Both diffusion-weighted (DW) and DT-CMR take advantage of the Brownian motion of water molecules in myocardial tissue (cardiomyocytes and extracellular matrix) to provide measurements about the myocardial tissue's underlying microstructural organization.[96]

DT-CMR relies on information obtained from DW images. By using strong bipolar gradients (diffusion gradients) to sensitize the MR signal to the diffusivity of water molecules, DW imaging generates a number of images with different degrees of diffusion weighing based on the b-values (units of seconds per mm^2). Typical b-values range from 450 to 600 s/mm^2 and reflect the gradient amplitude, duration, and temporal separation between the gradient pulses. The water diffusivity along a particular spatial direction can be calculated by performing an exponential fit on the signal intensities from the DW images. For DT-CMR, the 3D diffusion tensor is calculated from DW images with multi-directional diffusion encoding gradients. DT-CMR *in vivo* data can be acquired using 1) cardiac and respiratory dual-gated stimulated echo pulse sequences such as STEAM,[95, 97] 2) velocity-compensated (M1 gradient moment nulled) and/or acceleration-compensated (M2 gradient moment nulled) spin echo (SE) echo-planar imaging (EPI) sequences,[98–101] or 3) SE-EPI techniques with post-processing using principal component analysis for motion filtering.[102] M1/M2-nulled approaches use motion-compensated diffusion encoding gradients to reduce signal phase errors and signal void caused by cardiac motion; these techniques however, inevitably increase the echo time and further reduce the SNR. STEAM does not require high performance gradients because a significant contribution to the b value comes from the long mixing time in STEAM rather than from the strong bipolar gradients in conventional SE-EPI approaches.[96] STEAM however, can be sensitive to relative motion that occurs between the time of the stimulated echo encoding and the time of the diffusion readout, which happens one heartbeat later. Therefore, it is crucial to ensure that the heart is in the same breathing position and at the same time point within the cardiac cycle between these two successive heartbeats. This may be achieved using ECG-gating and navigator-based respiratory gating. [97] In a typical STEAM scan, for every 2D slice, eight breath-held images are acquired over ~18 heart beats and averaged. The images are post-processed using proprietary software algorithms to generate 3D diffusion tensor maps that reflect different components of myocyte organization and behavior. Several recent clinical research studies[103–106] conducted in small groups of normal volunteers and patients have relied on STEAM. Pathologies included hypertrophic cardiomyopathy, dilated cardiomyopathy, myocardial infarction, congenital heart disease, and amyloidosis.[96, 106] Due to the intrinsic 50% SNR loss when stimulated echoes are acquired, STEAM has relatively lower SNR than single-shot SE-EPI acquisitions using similar pulse sequence parameters, which may be compensated by incorporating larger voxel sizes (e.g. $2.8 \times 2.8 \times 8$ mm^2).[105] Moreover, STEAM is dependent on two regular R-R intervals, is less applicable to patients with dysrhythmia, and is susceptible to confounding effects of myocardial deformation due to the long diffusion time.

Several quantitative DT-CMR parameters merit discussion because of their physiological and clinical implications in structure-function relationships. DT-CMR relies on a 3D eigensystem whereby the *eigenvalues* (λ_1, λ_2, λ_3) describe the magnitude of directional

diffusivity and the *eigenvectors* (E1, E2, E3) describe the direction (Fig. 4). E1 is the principle eigenvector and corresponds to the average intravoxel cardiomyocyte orientation while E2 reflects the predominant sheetlet orientation and E3 reflects the normal sheetlet orientation.[107–110] The average eigenvector is represented by each imaging voxel and 3D diffusion maps convey pixelwise information. *Mean diffusivity* (MD) is similar to mean apparent diffusion coefficient (ADC) from DW imaging and reflects the average of the eigenvalues. MD represents the packing of myocytes; low values indicate tight packing and higher values indicate greater interstitial pathology. *Fractional anisotropy* (FA) values parallel changes in tissue organization; a low FA may indicate greater myocyte disarray. Using DT-CMR, MD and FA values can differentiate between cardiac amyloidosis and hypertrophic cardiomyopathy.[106] MD and FA are scalar diffusivity parameters and are reported as global values across the mid-ventricle in healthy volunteers; they can vary depending on the pulse sequence, cardiac phase, and b-values used during the image acquisition. Cardiomyocyte orientation is described using the *helix angle* (HA, E1A), which is the angulation created by E1 and the circumferential direction (Fig. 4). Sheetlet orientation is described by E2A, which is the angulation between E2 projected onto the cross-myocyte plane. In healthy myocardium, FA is highest in the mid-myocardium (0.46 ± 0.04) relative to the endo- (0.40 ± 0.04) and epicardium (0.39 ± 0.004).[104] MD exhibits a transmural gradient that increases from epicardium ($0.87\pm0.07\times10^{-3}$ mm^2/s) to endocardium ($0.91\pm0.08\times10^{-3}$ mm^2/s).[111] Transmural gradient of the HA reflecting cardiomyocyte orientation is small (transverse angle is between $-20°$ to $+20°$).[110] Sheetlet orientation (E2A) however, varies throughout the cardiac cycle and is likely due to radial strain. Biphasic E2A variation is present using STEAM:[112] $26\pm6°$ in diastole, $54\pm6°$ in systole. Together, measures of diffusivity, cardiomyocyte orientation, and sheetlet orientation, can characterize dynamic microstructural alterations that affect the overall ventricular geometry and function (Fig. 5).

4D INTRACARDIAC BLOOD FLOW

Ventricular geometry or shape is influenced by the impact of intracardiac blood flow over time. To preserve energy during the cardiac cycle, blood flow through the ventricle generates vortices. These intraventricular blood flow vortices are affected by changes in ventricular geometry and have different formation time, size, shape, strength, depth, and direction based on cardiac structure and function. In heart failure patients, the intracardiac blood flow pattern is altered and has been shown to be associated with decreased preservation of LV inflow kinetic energy. These parameters lend insight about the impact of intracardiac blood flow on LV remodeling and overall function.

Recent advances in MR hardware and in image reconstruction and acceleration have enabled the clinical use of 4D flow CMR for visualization and quantification of vascular[113] and intracardiac blood flow and energy distribution.[114, 115] 4D flow phase contrast pulse sequences are typically non-breath-held because of long acquisition time (10–25 minutes). Several image acceleration techniques are used to reduce acquisition time and a variety of respiratory motion compensation or self-gating strategies are employed to cope with the additional time window required for adequate spatial and temporal resolution. A spatial resolution of $<3.0 \times 3.0 \times 3.0$ mm^3 with high temporal resolution is necessary for

quantification of intracardiac blood flow. The maximum flow velocity (or the velocity encoding sensitivity [VENC]) is typically set at 10% above the maximal expected velocity to avoid velocity aliasing. If the VENC is set too high, an increase in velocity noise may occur. To include both early and late diastolic filling, retrospective cardiac gating is used. Because several sources of error can lead to large discrepancies in 4D flow data, careful pre-processing may be needed. Major sources of error include eddy current effects, concomitant Maxwell field effects, gradient non-linearity, and phase wraps. Many of these errors are corrected inline by the reconstruction algorithms on the scanner software. If velocity aliasing occurs however, additional phase-unwrapping steps may be necessary. For quality control, quantitative verification based on the conservation of mass principle is also employed. A useful check is the consistency in net aortic and pulmonary artery outflow, which should be equal in the absence of intracardiac shunts. Another internal check of the acquired data is verification of 4D flow with a validated 2D phase-contrast scan.

Once acquired, 4D flow datasets can be reformatted to user-defined 2D views and blood flow information (velocity direction and magnitude, kinetic energy, and vorticity) is color coded using commercially available software. Data can be presented as 2D velocity vector or 2D streamline displays to reflect velocity direction. 3D visualization of intracardiac flow is also possible. Three emerging quantitative parameters of relevance for structure-function relationships include: 1) particle tracing quantification to evaluate blood volume transportation efficiency,[116, 117] 2) intracardiac kinetic energy quantification ($E = \frac{1}{2}mv^2$ where m=mass, v=velocity) for HF classification,[118–120] and 3) vortical flow.[121–123] as an indicator of maladaptive ventricular shape. The interplay among intracardiac blood volume transport efficiency, kinetic energy, and altered vortical flow is grounded in the physics of fluid dynamics and can be related to the mechanical function of the ventricle. Relative to patients with normal LV function, patients with impaired LV function have persistence of vortical flow (vortex formation) in both diastole and systole (Fig. 6).[124] Because particle tracing enables tracking of the 3D trajectory of blood volume (equal to the voxel size) over the entire cardiac cycle, blood flow components in healthy and pathologic states can be classified into direct flow, retained flow, delayed ejection, or residual volume. A higher percentage of direct flow is assumed to be associated with more efficient transport of intracardiac blood volume. In HF patients (n=34 dilated cardiomyopathy, n=30 ischemic cardiomyopathy, n=36 healthy volunteers), direct-flow average intracardiac kinetic energy had an independent predictive relationship with 6-minute walk distance (a prognostic measure of functional capacity, β=0.280, p=0.035; model R^2 0.466, p=0.002) but neither EF nor LV volumes were independently predictive.[125] In Fontan patients, both intracardiac kinetic energy and vortical flow are altered[126, 127] and in patients with total cavopulmonary connections, exercise capacity has been linked to energy loss.[128] With dobutamine-induced stress in Fontan patients, kinetic energy, viscous energy loss, and vorticity increases and percent change between rest-stress has negative correlation with VO_2 max (kinetic energy, r=−0.83, p=0.003; energy loss, r=−0.80, p=0.006; vorticity volume, r=−0.64, p=0.047).[128]

CONCLUSION

Diagnosis, prognosis, treatment, and development of new therapeutics require reliable imaging biomarkers of contractile function beyond the EF. With robust computational power, the development of image-based, multidimensional, patient-specific HF models that incorporate myocardial deformation, tissue microstructure, and intracardiac flow data to provide structure-function relationships is on the horizon. New CMR methods have potential to facilitate HF phenotyping by enabling more granular characterization of ventricular structure-function relationships. While exciting, a major limitation to widespread translation of CMR techniques is vendor adoption and commercialization. Until demand for such techniques follow market metrics and comparative-effectiveness studies with clinical outcomes data are available, many of the described developments will remain in the research realm and access will be limited to the few patients at medical centers with active technical CMR research and industry relationships.

Sources of Funding:

References

1. Benjamin EJ, Blaha MJ, Chiuve SE, et al. Heart Disease and Stroke Statistics-2017 Update: A Report From the American Heart Association. Circulation. 2017;135:e146–e603. [PubMed: 28122885]

2. Konstam MA and Abboud FM. Ejection Fraction: Misunderstood and Overrated (Changing the Paradigm in Categorizing Heart Failure). Circulation. 2017;135:717–719. [PubMed: 28223323]

3. Kennedy JW, Baxley WA, Figley MM, et al. Quantitative angiocardiography. I. The normal left ventricle in man. Circulation. 1966;34:272–8. [PubMed: 5969358]

4. Sonnenblick EH. Correlation of myocardial ultrastructure and function. Circulation. 1968;38:29–44. [PubMed: 11712290]

5. Ridgway JP. Cardiovascular magnetic resonance physics for clinicians: part I. J Cardiovasc Magn Reson. 2010;12:71. [PubMed: 21118531]

6. Biglands JD, Radjenovic A and Ridgway JP. Cardiovascular magnetic resonance physics for clinicians: Part II. J Cardiovasc Magn Reson. 2012;14:66. [PubMed: 22995744]

7. Schulz-Menger J, Bluemke DA, Bremerich J, et al. Standardized image interpretation and post-processing in cardiovascular magnetic resonance - 2020 update : Society for Cardiovascular Magnetic Resonance (SCMR): Board of Trustees Task Force on Standardized Post-Processing. J Cardiovasc Magn Reson. 2020;22:19. [PubMed: 32160925]

8. Kramer CM, Barkhausen J, Bucciarelli-Ducci C, et al. Standardized cardiovascular magnetic resonance imaging (CMR) protocols: 2020 update. J Cardiovasc Magn Reson. 2020;22:17. [PubMed: 32089132]

9. Streeter DD Jr., Spotnitz HM, Patel DP, et al. Fiber orientation in the canine left ventricle during diastole and systole. Circulation research. 1969;24:339–47. [PubMed: 5766515]

10. LeGrice IJ, Smaill BH, Chai LZ, et al. Laminar structure of the heart: ventricular myocyte arrangement and connective tissue architecture in the dog. The American journal of physiology. 1995;269:H571–82. [PubMed: 7653621]

11. Kung GL, Nguyen TC, Itoh A, et al. The presence of two local myocardial sheet populations confirmed by diffusion tensor MRI and histological validation. J Magn Reson Imaging. 2011;34:1080–91. [PubMed: 21932362]

12. Rocha BML, Cunha GJL and Menezes Falcão LF. The Burden of Iron Deficiency in Heart Failure: Therapeutic Approach. J Am Coll Cardiol. 2018;71:782–793. [PubMed: 29447741]

13. Ponikowski P, Voors AA, Anker SD, et al. 2016 ESC Guidelines for the diagnosis and treatment of acute and chronic heart failure: The Task Force for the diagnosis and treatment of acute and chronic heart failure of the European Society of Cardiology (ESC)Developed with the special contribution of the Heart Failure Association (HFA) of the ESC. European heart journal. 2016;37:2129–2200. [PubMed: 27206819]

14. Auerbach M, Gafter-Gvili A and Macdougall IC. Intravenous iron: a framework for changing the management of iron deficiency. The Lancet Haematology. 2020;7:e342–e350. [PubMed: 32220343]

15. Huckle JE, Altun E, Jay M, et al. Gadolinium Deposition in Humans: When Did We Learn That Gadolinium Was Deposited In Vivo? Invest Radiol. 2016;51:236–40. [PubMed: 26588463]

16. McDonald RJ, Levine D, Weinreb J, et al. Gadolinium Retention: A Research Roadmap from the 2018 NIH/ACR/RSNA Workshop on Gadolinium Chelates. Radiology. 2018:181151.

17. Auerbach M, Chertow GM and Rosner M. Ferumoxytol for the treatment of iron deficiency anemia. Expert review of hematology. 2018.

18. Neuwelt EA, Hamilton BE, Varallyay CG, et al. Ultrasmall superparamagnetic iron oxides (USPIOs): a future alternative magnetic resonance (MR) contrast agent for patients at risk for nephrogenic systemic fibrosis (NSF)? Kidney international. 2009;75:465–74. [PubMed: 18843256]

19. Bashir MR, Bhatti L, Marin D, et al. Emerging applications for ferumoxytol as a contrast agent in MRI. J Magn Reson Imaging. 2015 4;41:884–98. [PubMed: 24974785]

20. Finn JP, Nguyen KL, Han F, et al. Cardiovascular MRI with ferumoxytol. Clin Radiol. 2016;71:796–806. [PubMed: 27221526]

21. Toth GB, Varallyay CG, Horvath A, et al. Current and potential imaging applications of ferumoxytol for magnetic resonance imaging. Kidney international. 2017.

22. Anzai Y, Prince MR, Chenevert TL, et al. MR angiography with an ultrasmall superparamagnetic iron oxide blood pool agent. J Magn Reson Imaging. 1997;7:209–14. [PubMed: 9039617]

23. Prince MR, Zhang HL, Chabra SG, et al. A pilot investigation of new superparamagnetic iron oxide (ferumoxytol) as a contrast agent for cardiovascular MRI. Journal of X-ray science and technology. 2003;11:231–40. [PubMed: 22388293]

24. Nguyen KL, Shao J, Ghodrati VK, et al. P. Ferumoxytol-Enhanced CMR for Vasodilator Stress Testing: A Feasibility Study. JACC Cardiovascular imaging. 2019.

25. Alam SR, Shah AS, Richards J, et al. Ultrasmall superparamagnetic particles of iron oxide in patients with acute myocardial infarction: early clinical experience. Circulation Cardiovascular imaging. 2012;5:559–65. [PubMed: 22875883]

26. Alam SR, Stirrat C, Richards J, et al. E. Vascular and plaque imaging with ultrasmall superparamagnetic particles of iron oxide. J Cardiovasc Magn Reson. 2015;17:83. [PubMed: 26381872]

27. Stirrat CG, Alam SR, MacGillivray TJ, et al. Ferumoxytol-enhanced magnetic resonance imaging assessing inflammation after myocardial infarction. Heart. 2017;103:1528–1535. [PubMed: 28642288]

28. U.S. Food and Drug Administration. FDA Drug Safety Communication: FDA strengthens warnings and changes prescribing instructions to decrease the risk of serious allergic reactions with anemia drug Feraheme (ferumoxytol). 2015; Accessed March 30, 2015. http://www.fda.gov/Drugs/DrugSafety/ucm440138.htm.

29. Ning P, Zucker EJ, Wong P, et al. Hemodynamic safety and efficacy of ferumoxytol as an intravenous contrast agents in pediatric patients and young adults. Magnetic resonance imaging. 2016;34:152–8. [PubMed: 26518061]

30. Muehe AM, Feng D, von Eyben R, et al.. Safety Report of Ferumoxytol for Magnetic Resonance Imaging in Children and Young Adults. Invest Radiol. 2016;51:221–7. [PubMed: 26656202]

31. Nguyen KL, Yoshida T, Han F, et al. MRI with ferumoxytol: A single center experience of safety across the age spectrum. J Magn Reson Imaging. 2017 3;45(3):804–812. [Epub 2016 Aug 2]. [PubMed: 27480885]

32. Varallyay CG, Toth GB, Fu R, et al. What Does the Boxed Warning Tell Us? Safe Practice of Using Ferumoxytol as an MRI Contrast Agent. AJNR American journal of neuroradiology. 2017.

33. Nguyen KL, Yoshida T, Kathuria-Prakash N,et al. Multicenter Safety and Practice for Off-Label Diagnostic Use of Ferumoxytol in MRI. Radiology. 2019;293:554–564. [PubMed: 31638489]

34. Atkinson DJ and Edelman RR. Cineangiography of the heart in a single breath hold with a segmented turboFLASH sequence. Radiology. 1991;178:357–60. [PubMed: 1987592]

35. Carr JC, Simonetti O, Bundy J, et al. Cine MR angiography of the heart with segmented true fast imaging with steady-state precession. Radiology. 2001;219:828–34. [PubMed: 11376278]

36. Miller S, Simonetti OP, Carr J, et al. MR Imaging of the heart with cine true fast imaging with steady-state precession: influence of spatial and temporal resolutions on left ventricular functional parameters. Radiology. 2002;223:263–9. [PubMed: 11930076]

37. Moon JC, Lorenz CH, Francis JM, et al. Breath-hold FLASH and FISP cardiovascular MR imaging: left ventricular volume differences and reproducibility. Radiology. 2002;223:789–97. [PubMed: 12034951]

38. Plein S, Bloomer TN, Ridgway JP, et al. Steady-state free precession magnetic resonance imaging of the heart: comparison with segmented k-space gradient-echo imaging. J Magn Reson Imaging. 2001;14:230–6. [PubMed: 11536399]

39. Kozerke S and Plein S. Accelerated CMR using zonal, parallel and prior knowledge driven imaging methods. J Cardiovasc Magn Reson. 2008;10:29. [PubMed: 18534005]

40. Yang AC, Kretzler M, Sudarski S, et al. Sparse Reconstruction Techniques in Magnetic Resonance Imaging: Methods, Applications, and Challenges to Clinical Adoption. Invest Radiol. 2016;51:349–64. [PubMed: 27003227]

41. Bustin A, Fuin N, Botnar RM, et al. From Compressed-Sensing to Artificial Intelligence-Based Cardiac MRI Reconstruction. Front Cardiovasc Med. 2020;7:17. [PubMed: 32158767]

42. Tsao J, Boesiger P and Pruessmann KP. k-t BLAST and k-t SENSE: dynamic MRI with high frame rate exploiting spatiotemporal correlations. Magn Reson Med. 2003;50:1031–42. [PubMed: 14587014]

43. Lustig M, Donoho D and Pauly JM. Sparse MRI: The application of compressed sensing for rapid MR imaging. Magn Reson Med. 2007;58:1182–95. [PubMed: 17969013]

44. Uecker M, Lai P, Murphy MJ, et al. ESPIRiT--an eigenvalue approach to autocalibrating parallel MRI: where SENSE meets GRAPPA. Magn Reson Med. 2014;71:990–1001. [PubMed: 23649942]

45. Vincenti G, Monney P, Chaptinel J, et al. Compressed sensing single-breath-hold CMR for fast quantification of LV function, volumes, and mass. JACC Cardiovascular imaging. 2014;7:882–92. [PubMed: 25129517]

46. Park J, Larson AC, Zhang Q, et al. 4D radial coronary artery imaging within a single breath-hold: cine angiography with phase-sensitive fat suppression (CAPS). Magn Reson Med. 2005;54:833–40. [PubMed: 16149060]

47. Kressler B, Spincemaille P, Nguyen TD, et al. Three-dimensional cine imaging using variable-density spiral trajectories and SSFP with application to coronary artery angiography. Magn Reson Med. 2007;58:535–43. [PubMed: 17763360]

48. Lai P, Larson AC, Park J, et al. Respiratory self-gated four-dimensional coronary MR angiography: a feasibility study. Magn Reson Med. 2008;59:1378–85. [PubMed: 18506786]

49. Liu J, Spincemaille P, Codella NC, et al. Respiratory and cardiac self-gated free-breathing cardiac CINE imaging with multiecho 3D hybrid radial SSFP acquisition. Magn Reson Med. 2010;63:1230–7. [PubMed: 20432294]

50. Liu J, Nguyen TD, Zhu Y, et al. Self-gated free-breathing 3D coronary CINE imaging with simultaneous water and fat visualization. PloS one. 2014;9:e89315. [PubMed: 24586682]

51. Coppo S, Piccini D, Bonanno G, et al. Free-running 4D whole-heart self-navigated golden angle MRI: Initial results. Magn Reson Med. 2015;74:1306–16. [PubMed: 25376772]

52. Han F, Rapacchi S, Khan S, et al. Four-dimensional, multiphase, steady-state imaging with contrast enhancement (MUSIC) in the heart: A feasibility study in children. Magn Reson Med. 2015 10;74:1042–1049. [PubMed: 25302932]

53. Han F, Zhou Z, Han E, et al. Self-gated 4D multiphase, steady-state imaging with contrast enhancement (MUSIC) using rotating cartesian K-space (ROCK): Validation in children with congenital heart disease. Magn Reson Med. 2016.

54. Nguyen KL, Han F, Zhou Z, et al. 4D MUSIC CMR: value-based imaging of neonates and infants with congenital heart disease. J Cardiovasc Magn Reson. 2017;19:40. [PubMed: 28366171]

55. Zhou Z, Han F, Rapacchi S, et al. Accelerated ferumoxytol-enhanced 4D multiphase, steady-state imaging with contrast enhancement (MUSIC) cardiovascular MRI: validation in pediatric congenital heart disease. NMR Biomed. 2017;30.

56. Moghari MH, Barthur A, Amaral ME, et al. Free-breathing whole-heart 3D cine magnetic resonance imaging with prospective respiratory motion compensation. Magn Reson Med. 2018;80:181–189. [PubMed: 29222852]

57. Moghari MH, Uecker M, Roujol S, et al. Accelerated whole-heart MR angiography using a variable-density poisson-disc undersampling pattern and compressed sensing reconstruction. Magn Reson Med. 2018;79:761–769. [PubMed: 28497620]

58. Bustin A, Ginami G, Cruz G, et al. Five-minute whole-heart coronary MRA with sub-millimeter isotropic resolution, 100% respiratory scan efficiency, and 3D-PROST reconstruction. Magn Reson Med. 2019;81:102–115. [PubMed: 30058252]

59. Usman M, Ruijsink B, Nazir MS, et al. Free breathing whole-heart 3D CINE MRI with self-gated Cartesian trajectory. Magnetic resonance imaging. 2017;38:129–137. [PubMed: 28034638]

60. Cheng JY, Hanneman K, Zhang T, et al. Comprehensive motion-compensated highly accelerated 4D flow MRI with ferumoxytol enhancement for pediatric congenital heart disease. J Magn Reson Imaging. 2015.

61. Cheng JY, Hanneman K, Zhang T, et al. Comprehensive motion-compensated highly accelerated 4D flow MRI with ferumoxytol enhancement for pediatric congenital heart disease. J Magn Reson Imaging. 2016;43:1355–68. [PubMed: 26646061]

62. Larson AC, Kellman P, Arai A, et al. Preliminary investigation of respiratory self-gating for free-breathing segmented cine MRI. Magn Reson Med. 2005;53:159–68. [PubMed: 15690515]

63. Larson AC, White RD, Laub G, et al. Self-gated cardiac cine MRI. Magn Reson Med. 2004;51:93–102. [PubMed: 14705049]

64. Uribe S, Muthurangu V, Boubertakh R, et al. Whole-heart cine MRI using real-time respiratory self-gating. Magn Reson Med. 2007;57:606–13. [PubMed: 17326164]

65. Zhou Z, Han F, Yoshida T, et al. Improved 4D cardiac functional assessment for pediatric patients using motion-weighted image reconstruction. Magma (New York, NY). 2018;31:747–756.

66. Fonseca CG, Backhaus M, Bluemke DA, et al. The Cardiac Atlas Project--an imaging database for computational modeling and statistical atlases of the heart. Bioinformatics. 2011;27:2288–95. [PubMed: 21737439]

67. Medrano-Gracia P, Cowan BR, Ambale-Venkatesh B, et al. Left ventricular shape variation in asymptomatic populations: the Multi-Ethnic Study of Atherosclerosis. J Cardiovasc Magn Reson. 2014;16:56. [PubMed: 25160814]

68. Feng L, Axel L, Chandarana H, et al. XD-GRASP: Golden-angle radial MRI with reconstruction of extra motion-state dimensions using compressed sensing. Magn Reson Med. 2016;75:775–88. [PubMed: 25809847]

69. Feng L, Grimm R, Block KT, et al. Golden-angle radial sparse parallel MRI: combination of compressed sensing, parallel imaging, and golden-angle radial sampling for fast and flexible dynamic volumetric MRI. Magn Reson Med. 2014;72:707–17. [PubMed: 24142845]

70. Feng L, Coppo S, Piccini D, et al. 5D whole-heart sparse MRI. Magn Reson Med. 2018;79:826–838. [PubMed: 28497486]

71. Cheng JY, Zhang T, Alley MT, et al. Comprehensive Multi-Dimensional MRI for the Simultaneous Assessment of Cardiopulmonary Anatomy and Physiology. Scientific reports. 2017;7:5330. [PubMed: 28706270]

72. Zhang S, Uecker M, Voit D, et al. Real-time cardiovascular magnetic resonance at high temporal resolution: radial FLASH with nonlinear inverse reconstruction. J Cardiovasc Magn Reson. 2010;12:39. [PubMed: 20615228]

73. Uecker M, Zhang S and Frahm J. Nonlinear inverse reconstruction for real-time MRI of the human heart using undersampled radial FLASH. Magn Reson Med. 2010;63:1456–62. [PubMed: 20512847]

74. Frahm J, Haase A and Matthaei D. Rapid NMR imaging of dynamic processes using the FLASH technique. Magn Reson Med. 1986;3:321–7. [PubMed: 3713496]

75. Breuer FA, Kellman P, Griswold MA, et al. Dynamic autocalibrated parallel imaging using temporal GRAPPA (TGRAPPA). Magn Reson Med. 2005;53:981–5. [PubMed: 15799044]

76. Feng L, Srichai MB, Lim RP, et al. Highly accelerated real-time cardiac cine MRI using k-t SPARSE-SENSE. Magn Reson Med. 2013;70:64–74. [PubMed: 22887290]

77. Kellman P, Chefd'hotel C, Lorenz CH, et al. High spatial and temporal resolution cardiac cine MRI from retrospective reconstruction of data acquired in real time using motion correction and resorting. Magn Reson Med. 2009;62:1557–64. [PubMed: 19780155]

78. Hansen MS, Sørensen TS, Arai AE, et al. Retrospective reconstruction of high temporal resolution cine images from real-time MRI using iterative motion correction. Magn Reson Med. 2012;68:741–50. [PubMed: 22190255]

79. Xue H, Kellman P, Larocca G, et al. High spatial and temporal resolution retrospective cine cardiovascular magnetic resonance from shortened free breathing real-time acquisitions. J Cardiovasc Magn Reson. 2013;15:102. [PubMed: 24228930]

80. Camargo GC, Erthal F, Sabioni L, et al. Real-time cardiac magnetic resonance cine imaging with sparse sampling and iterative reconstruction for left-ventricular measures: Comparison with gold-standard segmented steady-state free precession. Magnetic resonance imaging. 2017;38:138–144. [PubMed: 28065694]

81. Usman M, Atkinson D, Odille F, et al. Motion corrected compressed sensing for free-breathing dynamic cardiac MRI. Magn Reson Med. 2013;70:504–16. [PubMed: 22899104]

82. Kido T, Kido T, Nakamura M, Watanabe K, et al. Compressed sensing real-time cine cardiovascular magnetic resonance: accurate assessment of left ventricular function in a single-breath-hold. J Cardiovasc Magn Reson. 2016;18:50. [PubMed: 27553656]

83. Rahsepar AA, Saybasili H, Ghasemiesfe A, et al. Motion-Corrected Real-Time Cine Magnetic Resonance Imaging of the Heart: Initial Clinical Experience. Invest Radiol. 2018;53:35–44. [PubMed: 28857861]

84. Scatteia A, Baritussio A and Bucciarelli-Ducci C. Strain imaging using cardiac magnetic resonance. Heart failure reviews. 2017;22:465–476. [PubMed: 28620745]

85. Zerhouni EA, Parish DM, Rogers WJ, et al. Human heart: tagging with MR imaging--a method for noninvasive assessment of myocardial motion. Radiology. 1988;169:59–63. [PubMed: 3420283]

86. Ibrahim el SH. Myocardial tagging by cardiovascular magnetic resonance: evolution of techniques--pulse sequences, analysis algorithms, and applications. J Cardiovasc Magn Reson. 2011;13:36. [PubMed: 21798021]

87. Nasiraei-Moghaddam A and Finn JP. Tagging of cardiac magnetic resonance images in the polar coordinate system: Physical principles and practical implementation. Magn Reson Med. 2013.

88. Hor KN, Gottliebson WM, Carson C, et al. Comparison of magnetic resonance feature tracking for strain calculation with harmonic phase imaging analysis. JACC Cardiovascular imaging. 2010;3:144–51. [PubMed: 20159640]

89. Hor KN, Baumann R, Pedrizzetti G, et al. Magnetic resonance derived myocardial strain assessment using feature tracking. Journal of visualized experiments : JoVE. 2011.

90. Kammerlander AA, Donà C, Nitsche C, et al. Feature Tracking of Global Longitudinal Strain by Using Cardiovascular MRI Improves Risk Stratification in Heart Failure with Preserved Ejection Fraction. Radiology. 2020:200195.

91. Romano S, Judd RM, Kim RJ, et al. Feature-Tracking Global Longitudinal Strain Predicts Mortality in Patients With Preserved Ejection Fraction: A Multicenter Study. JACC Cardiovascular imaging. 2020;13:940–947. [PubMed: 31727563]

92. Romano S, Romer B, Evans K, et al. Prognostic Implications of Blunted Feature-Tracking Global Longitudinal Strain During Vasodilator Cardiovascular Magnetic Resonance Stress Imaging. JACC Cardiovascular imaging. 2020;13:58–65. [PubMed: 31005520]

93. Udelson JE. Left Ventricular Shape: The Forgotten Stepchild of Remodeling Parameters. JACC Heart failure. 2017;5:179–181. [PubMed: 28254123]

94. Udelson JE and Konstam MA. Relation between left ventricular remodeling and clinical outcomes in heart failure patients with left ventricular systolic dysfunction. Journal of cardiac failure. 2002;8:S465–71. [PubMed: 12555159]

95. Edelman RR, Gaa J, Wedeen VJ, et al. In vivo measurement of water diffusion in the human heart. Magn Reson Med. 1994;32:423–8. [PubMed: 7984077]

96. Nielles-Vallespin S, Scott A, Ferreira P, et al. Cardiac Diffusion: Technique and Practical Applications. J Magn Reson Imaging. 2019.

97. Nielles-Vallespin S, Mekkaoui C, Gatehouse P, et al. In vivo diffusion tensor MRI of the human heart: reproducibility of breath-hold and navigator-based approaches. Magn Reson Med. 2013;70:454–65. [PubMed: 23001828]

98. Nguyen C, Fan Z, Sharif B, et al. In vivo three-dimensional high resolution cardiac diffusion-weighted MRI: a motion compensated diffusion-prepared balanced steady-state free precession approach. Magn Reson Med. 2014;72:1257–67. [PubMed: 24259113]

99. Welsh CL, DiBella EV and Hsu EW. Higher-Order Motion-Compensation for In Vivo Cardiac Diffusion Tensor Imaging in Rats. IEEE transactions on medical imaging. 2015;34:1843–53. [PubMed: 25775486]

100. Stoeck CT, von Deuster C, Genet M, et al. Second-order motion-compensated spin echo diffusion tensor imaging of the human heart. Magn Reson Med. 2016;75:1669–76. [PubMed: 26033456]

101. Aliotta E, Wu HH and Ennis DB. Convex optimized diffusion encoding (CODE) gradient waveforms for minimum echo time and bulk motion-compensated diffusion-weighted MRI. Magn Reson Med. 2017;77:717–729. [PubMed: 26900872]

102. Delattre BM, Viallon M, Wei H, et al. In vivo cardiac diffusion-weighted magnetic resonance imaging: quantification of normal perfusion and diffusion coefficients with intravoxel incoherent motion imaging. Invest Radiol. 2012;47:662–70. [PubMed: 23001045]

103. Ferreira PF, Kilner PJ, McGill LA, et al. In vivo cardiovascular magnetic resonance diffusion tensor imaging shows evidence of abnormal myocardial laminar orientations and mobility in hypertrophic cardiomyopathy. J Cardiovasc Magn Reson. 2014;16:87. [PubMed: 25388867]

104. McGill LA, Scott AD, Ferreira PF, et al. Heterogeneity of Fractional Anisotropy and Mean Diffusivity Measurements by In Vivo Diffusion Tensor Imaging in Normal Human Hearts. PloS one. 2015;10:e0132360. [PubMed: 26177211]

105. Nielles-Vallespin S, Khalique Z, Ferreira PF, et al. Assessment of Myocardial Microstructural Dynamics by In Vivo Diffusion Tensor Cardiac Magnetic Resonance. J Am Coll Cardiol. 2017;69:661–676. [PubMed: 28183509]

106. Khalique Z, Ferreira PF, Scott AD, et al. Diffusion Tensor Cardiovascular Magnetic Resonance in Cardiac Amyloidosis. Circulation Cardiovascular imaging. 2020;13:e009901. [PubMed: 32408830]

107. Hsu EW, Muzikant AL, Matulevicius SA, et al. Magnetic resonance myocardial fiber-orientation mapping with direct histological correlation. The American journal of physiology. 1998;274:H1627–34. [PubMed: 9612373]

108. Scollan DF, Holmes A, Winslow R, et al. Histological validation of myocardial microstructure obtained from diffusion tensor magnetic resonance imaging. The American journal of physiology. 1998;275:H2308–18. [PubMed: 9843833]

109. Tseng WY, Wedeen VJ, Reese TG, et al. Diffusion tensor MRI of myocardial fibers and sheets: correspondence with visible cut-face texture. J Magn Reson Imaging. 2003;17:31–42. [PubMed: 12500272]

110. Chen J, Liu W, Zhang H, et al. Regional ventricular wall thickening reflects changes in cardiac fiber and sheet structure during contraction: quantification with diffusion tensor MRI. American journal of physiology Heart and circulatory physiology. 2005;289:H1898–907. [PubMed: 16219812]

111. Pope AJ, Sands GB, Smaill BH, et al. Three-dimensional transmural organization of perimysial collagen in the heart. American journal of physiology Heart and circulatory physiology. 2008;295:H1243–h1252. [PubMed: 18641274]

112. McGill LA, Ferreira PF, Scott AD, et al. Relationship between cardiac diffusion tensor imaging parameters and anthropometrics in healthy volunteers. J Cardiovasc Magn Reson. 2016;18:2. [PubMed: 26738482]

113. Dyverfeldt P, Bissell M, Barker AJ, et al. 4D flow cardiovascular magnetic resonance consensus statement. J Cardiovasc Magn Reson. 2015;17:72. [PubMed: 26257141]

114. Crandon S, Elbaz MSM, Westenberg JJM, et al. Clinical applications of intra-cardiac four-dimensional flow cardiovascular magnetic resonance: A systematic review. International journal of cardiology. 2017;249:486–493. [PubMed: 28964555]

115. Zhong L, Schrauben EM, Garcia J, et al. Intracardiac 4D Flow MRI in Congenital Heart Disease: Recommendations on Behalf of the ISMRM Flow & Motion Study Group. J Magn Reson Imaging. 2019;50:677–681. [PubMed: 31317587]

116. Bolger AF, Heiberg E, Karlsson M, et al. Transit of blood flow through the human left ventricle mapped by cardiovascular magnetic resonance. J Cardiovasc Magn Reson. 2007;9:741–7. [PubMed: 17891610]

117. Wigström L, Ebbers T, Fyrenius A, et al. Particle trace visualization of intracardiac flow using time-resolved 3D phase contrast MRI. Magn Reson Med. 1999;41:793–9. [PubMed: 10332856]

118. Carlsson M, Heiberg E, Toger J, et al. Quantification of left and right ventricular kinetic energy using four-dimensional intracardiac magnetic resonance imaging flow measurements. American journal of physiology Heart and circulatory physiology. 2012;302:H893–900. [PubMed: 22180653]

119. Kanski M, Arvidsson PM, Töger J, et al. Left ventricular fluid kinetic energy time curves in heart failure from cardiovascular magnetic resonance 4D flow data. J Cardiovasc Magn Reson. 2015;17:111. [PubMed: 26685664]

120. Wong J, Chabiniok R, deVecchi A, et al. Age-related changes in intraventricular kinetic energy: a physiological or pathological adaptation? American journal of physiology Heart and circulatory physiology. 2016;310:H747–55. [PubMed: 26747496]

121. Töger J, Kanski M, Arvidsson PM, et al. Vortex-ring mixing as a measure of diastolic function of the human heart: Phantom validation and initial observations in healthy volunteers and patients with heart failure. J Magn Reson Imaging. 2016;43:1386–97. [PubMed: 26663607]

122. Töger J, Kanski M, Carlsson M, et al. Vortex ring formation in the left ventricle of the heart: analysis by 4D flow MRI and Lagrangian coherent structures. Annals of biomedical engineering. 2012;40:2652–62. [PubMed: 22805980]

123. Elbaz MS, Calkoen EE, Westenberg JJ, et al. Vortex flow during early and late left ventricular filling in normal subjects: quantitative characterization using retrospectively-gated 4D flow cardiovascular magnetic resonance and three-dimensional vortex core analysis. J Cardiovasc Magn Reson. 2014;16:78. [PubMed: 25270083]

124. Suwa K, Saitoh T, Takehara Y, et al. Intra-left ventricular flow dynamics in patients with preserved and impaired left ventricular function: Analysis with 3D cine phase contrast MRI (4D-Flow). J Magn Reson Imaging. 2016;44:1493–1503. [PubMed: 27185516]

125. Stoll VM, Hess AT, Rodgers CT, et al. Left Ventricular Flow Analysis. Circulation Cardiovascular imaging. 2019;12:e008130. [PubMed: 31109184]

126. Sjöberg P, Heiberg E, Wingren P, et al. Decreased Diastolic Ventricular Kinetic Energy in Young Patients with Fontan Circulation Demonstrated by Four-Dimensional Cardiac Magnetic Resonance Imaging. Pediatr Cardiol. 2017;38:669–680. [PubMed: 28184976]

127. Kamphuis VP, Elbaz MSM, van den Boogaard PJ, et al. Disproportionate intraventricular viscous energy loss in Fontan patients: analysis by 4D flow MRI. European heart journal cardiovascular Imaging. 2019;20:323–333. [PubMed: 30060051]

128. Kamphuis VP, Elbaz MSM, van den Boogaard PJ, et al. Stress increases intracardiac 4D flow cardiovascular magnetic resonance -derived energetics and vorticity and relates to VO(2)max in Fontan patients. J Cardiovasc Magn Reson. 2019;21:43. [PubMed: 31340834]

KEY POINTS

- Novel cardiovascular magnetic resonance (CMR) approaches enable characterization of ventricular structure-function relationships in heart failure patients beyond the ventricular ejection fraction.

- Because heart failure patients are frequently anemic, theranostic use of ferumoxytol may address anemia and improve CMR imaging by facilitating steady-state contrast-enhanced image acquisition.

- Technical developments for functional imaging include a shift from 2-dimensional multislice cine acquisition to 5-dimensional imaging, which may enable simultaneous evaluation of cardiopulmonary physiology.

- Tissue motion mapping using feature tracking CMR has emerged as a clinically useful tool for myocardial strain quantification and has gained traction beyond conventional myocardial tagging and tissue velocity mapping methods.

- Diffusion tensor and intracardiac 4D flow mapping are promising techniques for characterization of tissue microstructure and evaluation of intracardiac blood flow's impact on ventricular morphology.
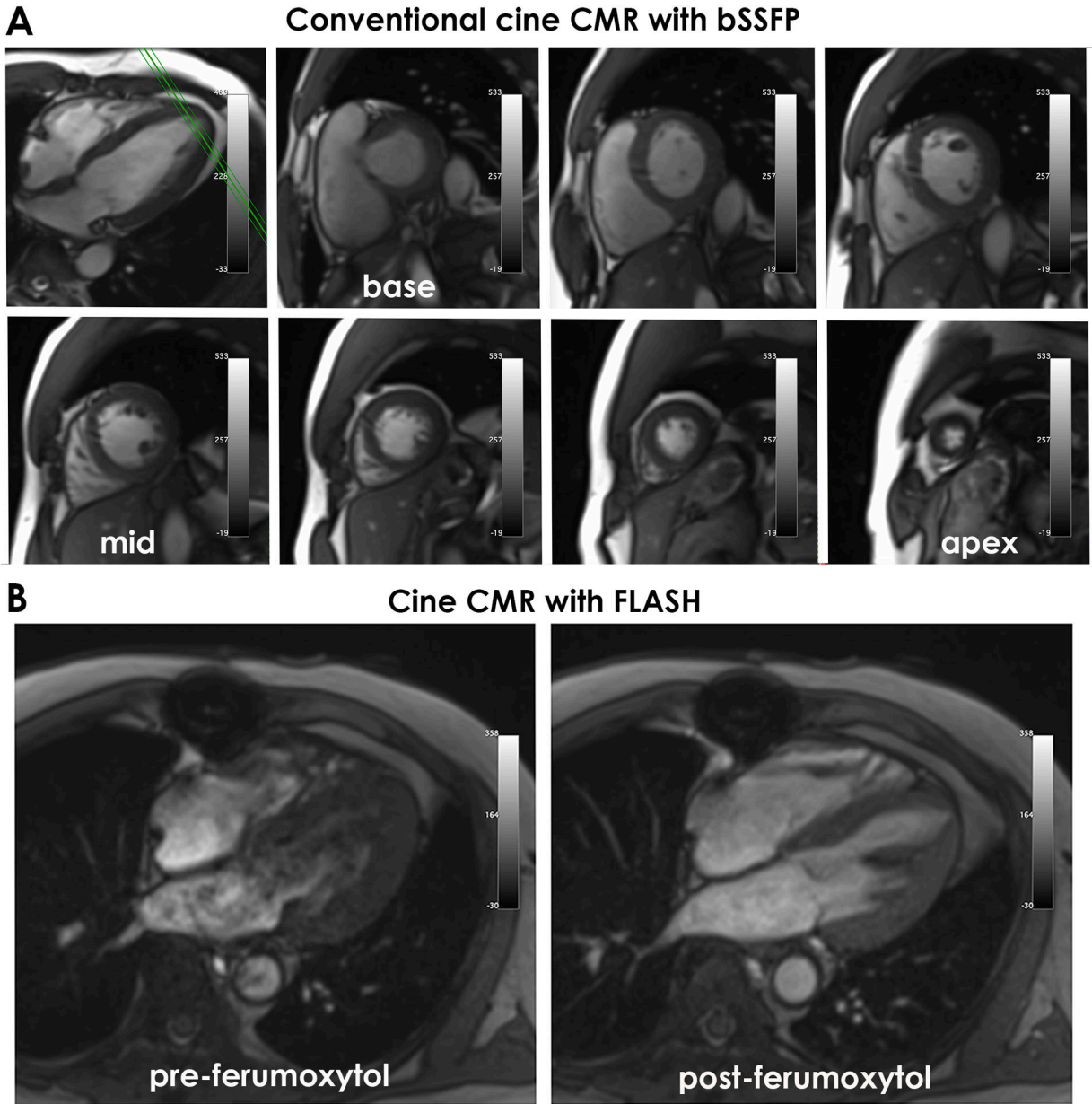
Fig. 1.
Quantification of left ventricular ejection fraction, volume, and mass can be accomplished using non-contrast cine CMR using a balanced steady-state free precession pulse sequence (bSSFP) (A) or from a fast low-angle single-shot (FLASH) (B) sequence. Using a long-axis image (A, upper left panel), multislice 2D short-axis images from base to apex are acquired perpendicular to the long-axis and then segmented offline to derive measures of left ventricular function (ejection fraction, volume, mass). Relative to non-contrast cine CMR images obtained from FLASH (B, left panel), ferumoxytol-enhanced cine FLASH CMR images (B, right panel) have improved image quality with less artifacts and more homogenous blood-pool.
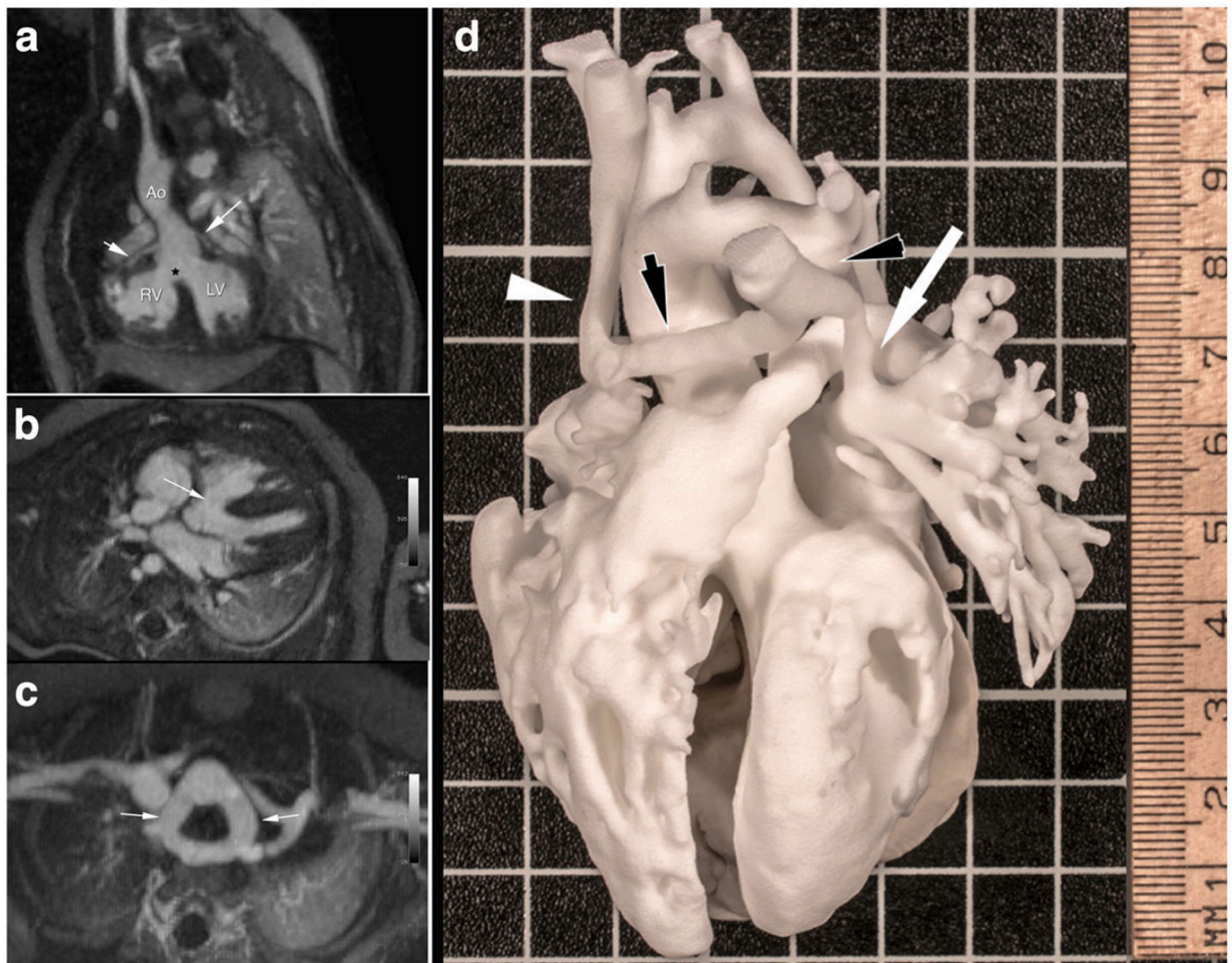
Fig. 2.
Ferumoxytol-enhanced 4D MUSIC CMR. Multiplanar reformats of 4D MUSIC in a three-month old girl (7.7 kg) with Tetralogy of Fallot (ToF) and a double aortic arch. (A) Characteristic features of ToF including right ventricular (RV) hypertrophy with dynamic RV outflow tract obstruction, an overriding aorta, and a perimembranous ventricular septal defect (black asterisk) are clearly visualized on dynamic review (Online movie 1A). Both proximal courses of the left and right coronary arteries (A, white arrow) are also well visualized; the distal right coronary artery can also be seen coursing along the right ventricle. (B) The large ventricular septal defect (B, white arrow) and the double aortic arch forming a complete vascular ring (C) are clearly delineated, without dynamic compression of the trachea (Online movie 1B). (D) 3D print shows anomalous pulmonary venous drainage with the left innominate vein (D, black arrow) dipping inferiorly before joining the right innominate vein (D, white arrowhead) to form a right-sided superior vena cava. The left superior vertical vein (D, black arrowhead) joins the low bridging left innominate vein (D, black arrow) and the left superior pulmonary vein (D, white arrow), which forms the confluence of the superior pulmonary venous trunk (Online movie 1A). Reprint from Nguyen KL, Han F, Zhou Z et al. 4D MUSIC CMR: Value-based Imaging of Neonates and

Infants with Congenital Heart Disease. *J Cardiovasc Magn Reson* 19, 40 (2017); with permission. (Figure 6 in original).
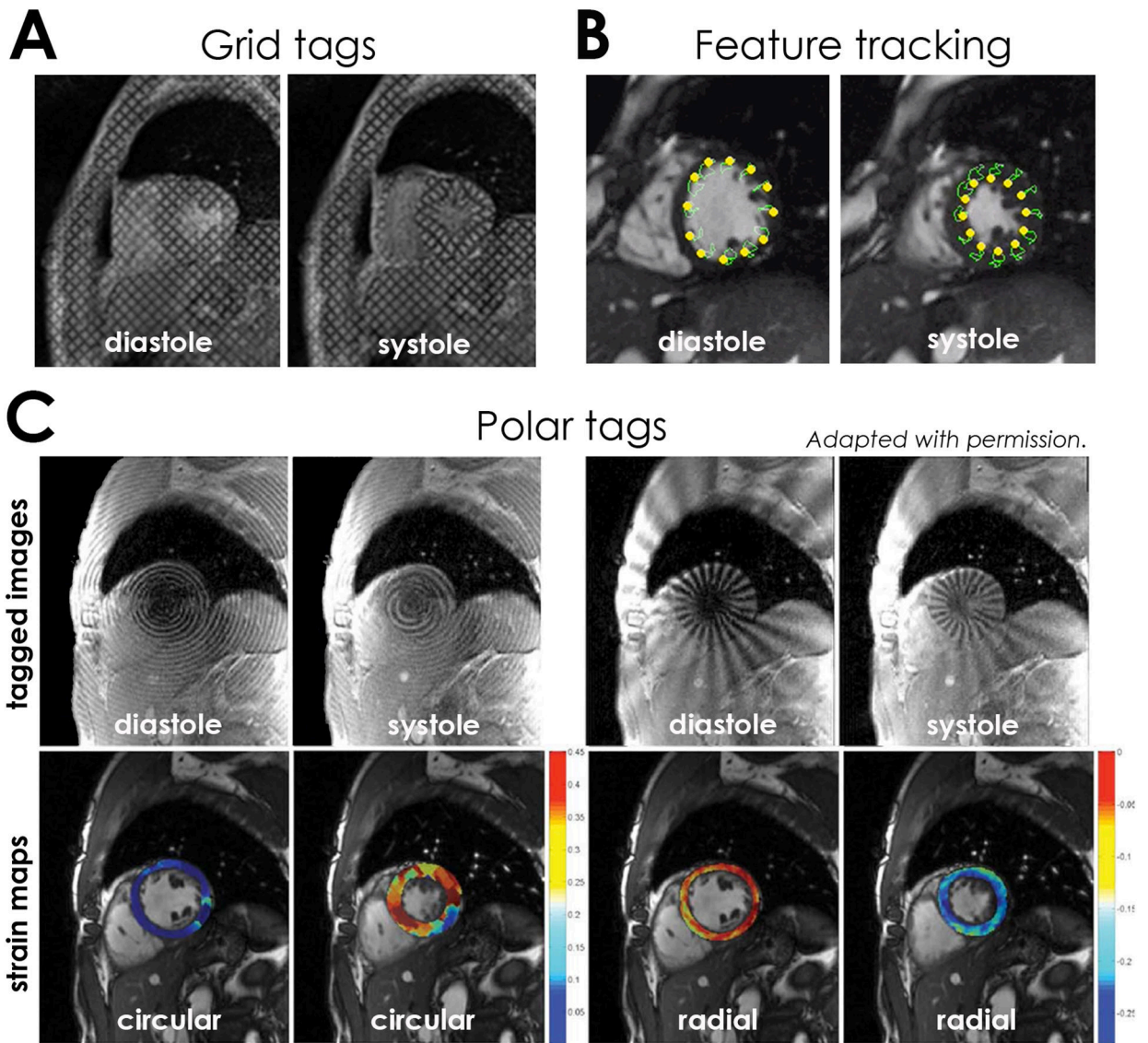
Fig. 3.
Myocardial mechanics can be quantified using rectilinear grid tags (A), feature tracking (B), or polar tags (C) in the circular and radial directions. Global and regional strain curves can be used to derive longitudinal, circumferential, and radial strain and strain rate. Rotational mechanics (torsion) is quantified using short-axis images. Panel C is adapted from Nasiraei-Moghaddam A, Finn JP. Tagging of cardiac magnetic resonance images in the polar coordinate system: physical principles and practical implementation; with permission. *Magn Reson Med.* 2014;71:1750–9. (Figure 6 in original)
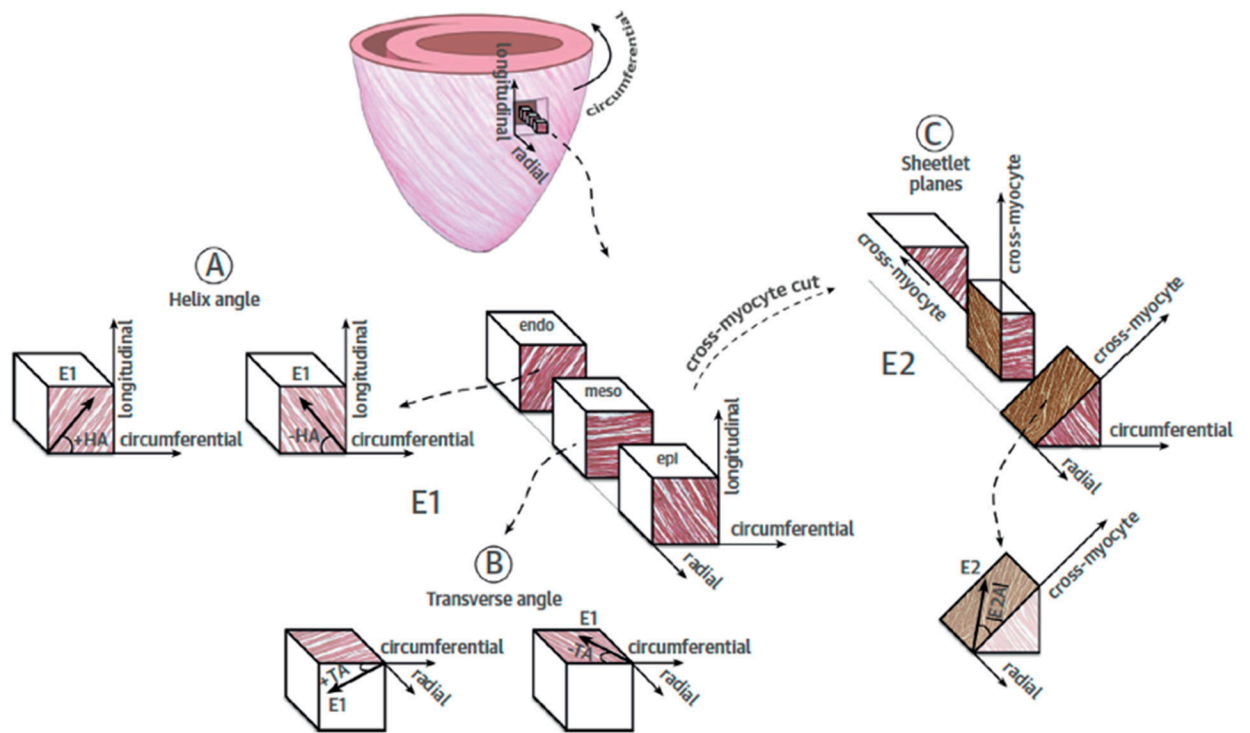
Fig. 4.
Eigenvectors Projected onto Cardiac Plane. The primary eigenvector (E1) is projected on the circumferential-longitudinal plane giving rise to the helix angle (HA) (A). E1 is projected on the circumferential-radial plane giving rise to the transverse angle (B). The voxels are cut in a cross-myocyte direction, showing the plane perpendicular to E1 (C). Projecting the second eigenvector (E2) onto the sheetlet plane gives E2A. From Khalique Z, Ferreira PF, Scott AD et al. Diffusion Tensor Cardiovascular Magnetic Resonance Imaging: A Clinical Perspective. *JACC Cardiovascular imaging.* 2020;13:1235–1255; with permission. (Figure 9 in original)
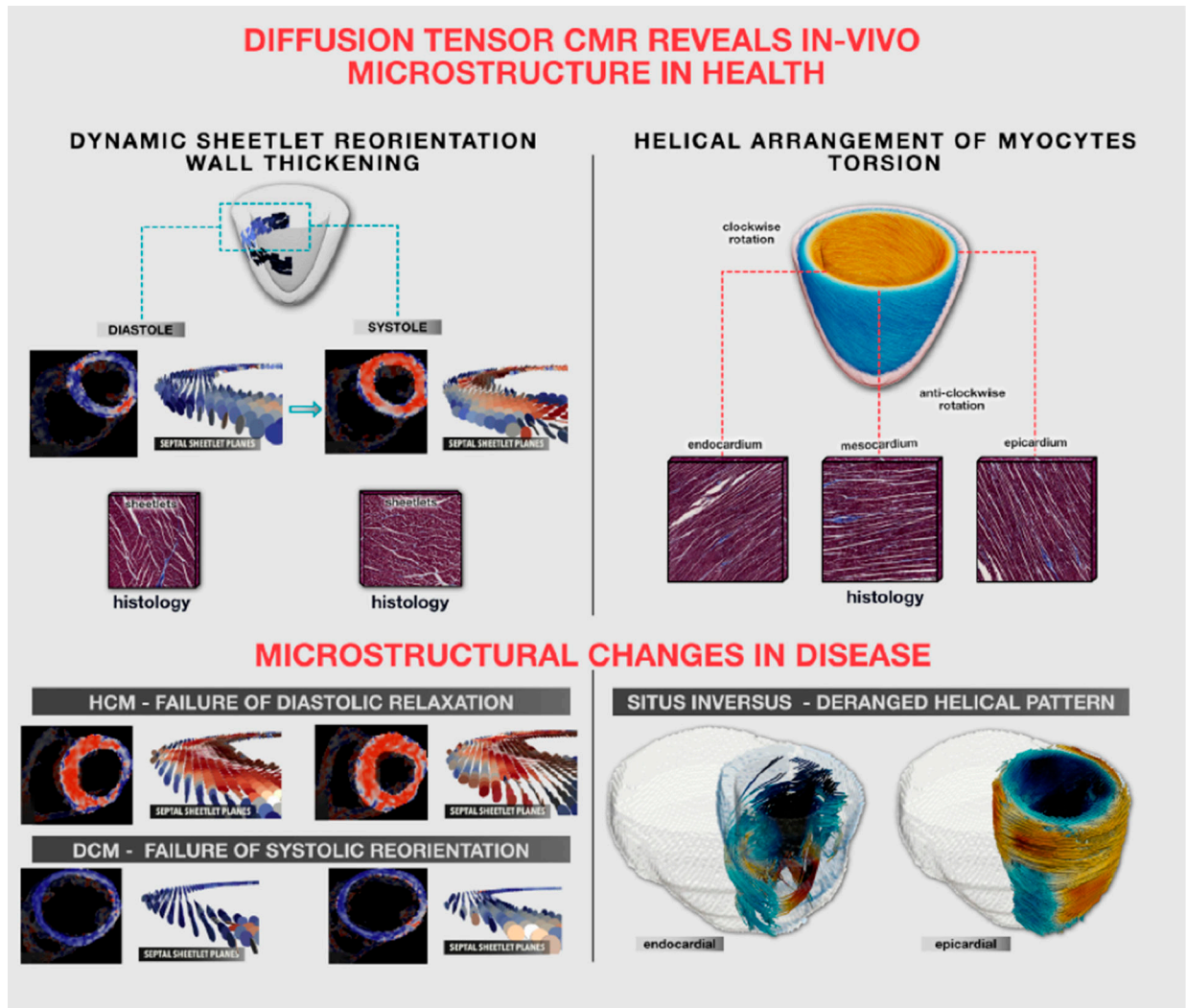
Fig. 5.
Diffusion tensor CMR (DT-CMR) in Health and in Disease States. In healthy left ventricles (LV), DT-CMR demonstrates reorientation of cardiomyocyte sheetlets from "wall-parallel" in diastole to "wall-perpendicular" in systole to cause LV wall thickening responsible for the predominant contraction (*upper left panel*). Sheetlets in hypertrophic cardiomyopathy (HCM) fail to relax to the expected diastolic position, whereas in dilated cardiomyopathy (DCM), sheetlets fail to rotate to the expected systolic position (*lower left panel*). DT-CMR demonstrates the helical arrangement of cardiomyocytes, with a right-handed helix in the endocardium, circumferential in the mesocardium, and left-handed helix in the epicardium (*upper right panel*). Contraction drives clockwise rotation basally and anti-clockwise rotation apically, resulting in left ventricular torsion. In patients with situs inversus, torsion is impaired (*lower right panel*). From Khalique Z, Ferreira PF, Scott AD et al. Diffusion Tensor Cardiovascular Magnetic Resonance Imaging: A Clinical Perspective. *JACC Cardiovascular imaging.* 2020;13:1235–1255; with permission. (Central Illustration in original)
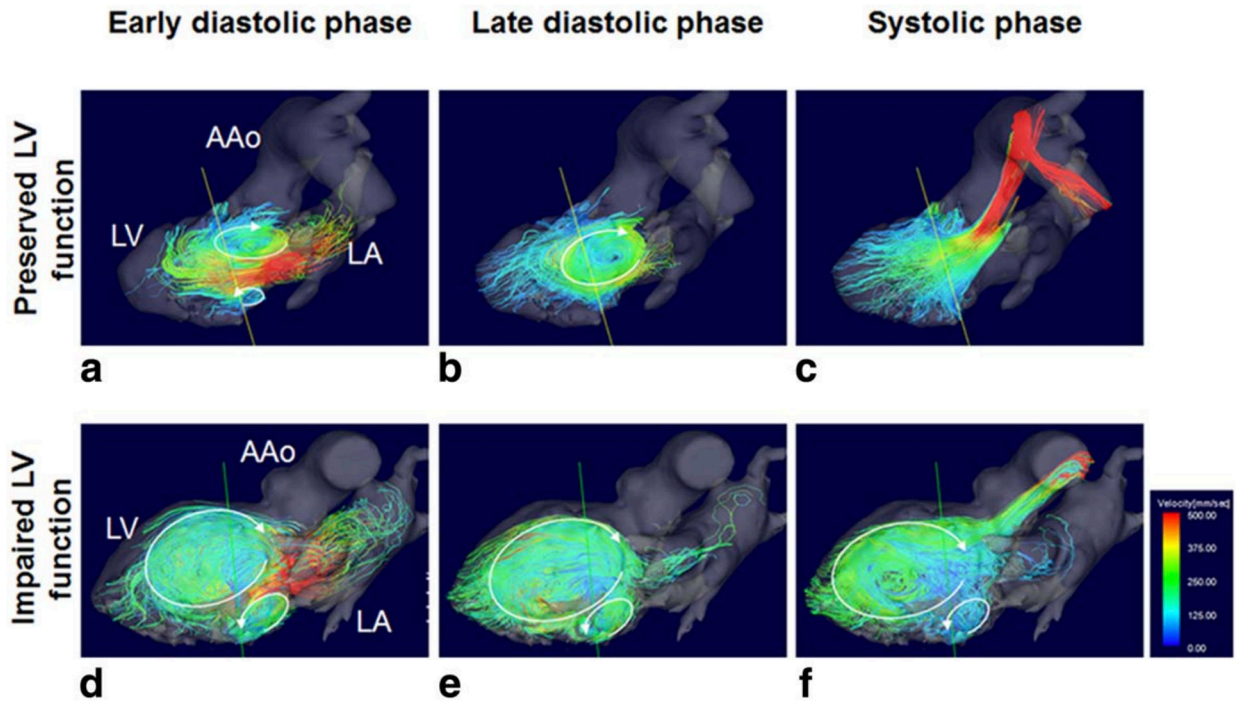
Fig. 6.
Color-rendered Streamline 4D Flow CMR Images with Intraventricular Vortex Patterns. Relative to a patient with normal left ventricular (LV) function (*upper panel*), the patient with reduced LV function (*lower panel*) has altered vortical flow (white circular arrow(s)) throughout of the cardiac cycle (early diastole, late diastole, and during systole). Note the absence of vortex formation during systole in the setting of normal LV function and persistence of vortex formation during systole in the setting of impaired LV function. From Suwa K, Saitoh T, Takehara Y, et al. Intra-left ventricular flow dynamics in patients with preserved and impaired left ventricular function: Analysis with 3D cine phase contrast MRI (4D-Flow). *J Magn Reson Imaging*. 2016;44:1493–1503.; with permission. (Figure 1 in original)

Movie 1:

4D cine MUSIC image of the same patient in Figure 2 demonstrate the complex intra-cardiac characteristic features of Tetralogy of Fallot (Movie 1A). Dynamic complex extra-cardiac vascular anatomy and its relationship to intra-cardiac structures are exemplified in Video 1A with colorized volume rendered 4D cine images. There is anomalous pulmonary venous drainage with the left innominate vein dipping inferiorly before joining the right innominate vein to form a right-sided superior vena cava. The left superior vertical vein joins the low bridging left innominate vein and the left superior pulmonary vein, which forms the confluence of the superior pulmonary venous trunk (Movie 1B, left panel). There is also a double aortic arch, which forms a complete vascular ring without tracheal compression (Movie 1B, right panel).